The Influence of Rotating Cage Geometry and Baffles on the Wall Shear Stress Equation in Sweet/Sour Corrosion

Rhuan C. Souza[a]* , Bernardo Coelho[a], Jefferson R. Oliveira[b], Gustavo L. Vaz[b],

André L.C. Bonfim[b], José Antônio C.P. Gomes[c] , Guillermo Vilalta-Alonso[a], Alysson H.S. Bueno[a]

[a]Universidade Federal de São João del Rei, São João del Rei, MG, Brasil.
[b]Centro de Pesquisa da Petrobras (CENPES), Rio de Janeiro, RJ, Brasil.
[c]Universidade Federal do Rio de Janeiro, Rio de Janeiro, RJ, Brasil.

Flow-accelerated corrosion has been studied by means of computational fluid dynamics (CFD) techniques and rotating cage (RC) autoclave tests according to ASTM G170. This study evaluated through CFD and laboratory tests the influence of RC geometry and baffles on the wall shear stress (τ_w) proposed by the aforementioned standard. The experimental were performed at 120 °C and 2 angular velocities (500 and 800 rpm) during 25 h in a solution with 600 mg/L of Cl$^-$ ions and 10^{-3} mol/L of sodium thiosulfate. Corrosion rates were obtained by ASTM G31 and the surfaces were evaluated by OM and XRD. Corrosion rate values and XRD analyses showed divergence between samples in different positions in the RC and between distinct regions in the same sample. The numerical simulations and the experimental tests showed a great influence of the baffles on τ_w. The conservatism in the values obtained with this technique is caused by excessive corrosion close to the samples edges and the non-uniformity of τ_w on the internal samples surfaces. Thus, the main conclusion of the study is related to the importance of better knowledge on experimental methodology and mathematical approximations for updating the criterion for the correct τ_w calculation on sample surfaces.

Keywords: Flow accelerated corrosion, rotating cage autoclave, CFD, API X65 steel, CO_2/H_2S.

1. Introduction

Damage caused in carbon steels pipelines by different corrosive mechanisms and turbulent fluid transport are a serious problem in oil and gas industry[1,2]. However, these materials are widely used in pipes manufacture due to its excellent cost-benefit ratio[1,3-6].

Among the oil and gas corrosive contaminants are carbon dioxide (CO_2) and hydrogen sulfide (H_2S)[7-10], their presence in pipeline systems generates the sweet/sour corrosion mechanism. When CO_2 and H_2S hydrates inside the wells, it dissociates and forms carbonic acid and hydrogen sulfide ionization species[11]. Then, iron carbonate ($FeCO_3$) and/or iron sulfide (FeS) films formed on the anodic steel surface, can reduce the kinetics of corrosive processes[10,12], or presenting non-protective characteristics, inducing new corrosion mechanisms in the system[13].

Internal flow in pipelines generates wall shear stresses, contributing to the flow accelerated corrosion (FAC) mechanism. Most often, the flow regime is turbulent, increasing the mass transport of corrosive species toward the metal surface[14,15]. The study of these systems is carried out using simulation by CFD and experimental tests with autoclaves. The rotating cage autoclave (RC) is one of the most

promising methodologies for simulating pipeline corrosion in laboratory[16-18]. One of the RC advantages is the vast range of possible and applicable shear stresses on specimens, may vary from 20 Pa to 200 Pa[16]. ASTM G170 standard[19] specifies the equations for a maximum wall shear stress:

$$\tau_w = 0,0791.Re^{-0,3}.\rho r^2.\omega^{2,3} \tag{1}$$

$$Re = \frac{2\rho\omega r^2}{\mu} \tag{2}$$

Where r is the cage radius (m), Re is Reynolds number, ρ is the fluid density (kg/m^3), ω is the angular speed (rad/s) and μ is dynamic viscosity (kg/m.s). The mathematics or experimental procedures, used by Papavinasam[20], proposed this equation that is not found in the literature, highlighting a gap in understanding the results of τ_w for RC.

The aim of this study is to evaluate the possibility of improvements in experimental configurations and equations currently used in RC tests. Then, it was carried out the CFD simulations with experimental tests in order to discuss the equation and approximates it with the real values obtained in experimental tests. The goal is to obtain a better distribution of wall shear stresses and consequently to approximate the laboratory results with those found in field.

*e-mail: rhuanmecufsj@gmail.com

2. Methodology

2.1. Computational fluid dynamic simulations

Considering the rotating cage used in experimental tests, 2 cases were created. The major difference between them is the presence or not of baffles for vortex prevention. Some details of the geometries, such as screws, chamfers and high reliefs, were ignored in order to reduce computational cost and simulation time.

The meshes of both geometries were created by using the sliding mesh approach (SM) for simulating the motion of rotating cage inside an autoclave. In SM model, 2 computational grids are used: one moving along with the cage and the other fixed to the vessel.

The application of the SM model made it possible to obtain a discretized domain with 1.223.643 hybrid elements for RC with baffles and 521.095 hybrid elements for RC with no baffles. In both cases, the region near to specimens was refined. Figure 1 shows the 2 meshes created. Due to the lack of computational power, a mesh independence test was not performed.

Three numerical simulations were carried out, being one at 800 rpm in the baffled geometry, two at 500 rpm in the baffled and non-baffled geometries. The Eulerian-Eulerian formulation was used to account the liquid-gas interaction along with the Realizable k-epsilon model, where turbulence equations were solved for each phase. Both fluids were assumed incompressible and their properties at 120 °C and 500 kPa (5 bar) (gauge) were used in the calculations.

Non-slip boundary conditions were applied at the walls and Standard Wall Functions were used to account high gradients near these regions.

The Phased Coupled SIMPLE algorithm was used for the pressure-velocity coupling and the Second Order Implicit Method for time advancement with a time step selected to maintain the Courant number below one.

2.1. Experimental tests

A corrosive, dynamic environment was evaluated, simulating flow in pipes and CO_2/H_2S environment. It used 4 API X65 carbon steel samples in the rotating cage (RC), with dimensions of 30 mm x 20 mm x 2 mm, grounded with
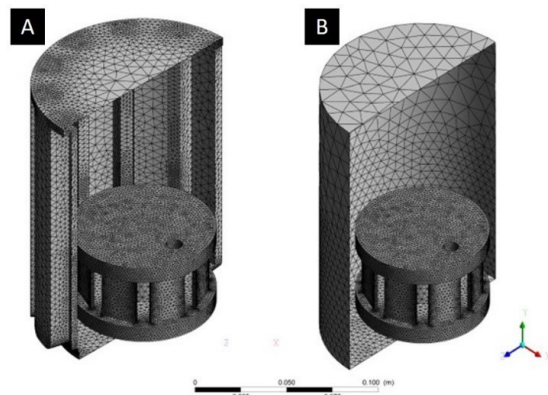
Figure 1. Mesh of the RC used: with baffles for vortex prevention (A); without baffles (B).

SiC paper up to 600 grit. They were positioned according to RC magnification in the autoclave scheme (Figure 2). The tests were performed at 500 rpm and 800 rpm for 25 h in 1 L of solution containing 600 mg/L of Cl^- ions, 10^{-3} mol/L of sodium thiosulfate, at 120 °C and 500 kPa (5 bar) (gauge) of CO_2. In this conditions, the fluid physical properties are ρ = 943.21 kg/m³ and μ = 0.0024605 Pa-s. The RC used consists of 2 PEEK discs of 80 mm in diameter, spaced between them in 30 mm, each with a vertical hole of 9 mm.

2.2. Material characterization

Initially the samples were analyzed by optical microscopy (OM) with an optical microscope Olympus model BX51, grounded with SiC paper up to 1500 grit, polished with alumina 1 μm and 0.3 μm and attacked with Nital solution 3% for 10 s. After immersion tests, surfaces were characterized by X-ray diffraction (XRD) with the diffratometer Shimadzu XRD – 6000 and X-ray beams focusing in the samples with 2Θ ranging from 10 to 80°. The XRD analyses were performed on the central region of the inner and outer faces of each sample, and all phases identifications were made based on the crystallographic structure given by the AMCSD (American Mineralogist Crystal Structure Database).

2.3. Sulfide potentiometric titration and iron content measurement

Over the 25 hours of testing, three aliquots of the solution were collected at the intervals of 1 h, 12 h, and 25 h of immersion. These aliquots were used to measure pH, total iron, and perform a potentiometric titration to calculate the concentration of H_2S generated during the test time.

The samples were drawn through valve 11 in Figure 2. A PEEK device allowed a pH electrode to be placed in contact with the withdrawn solution just after valve 11.

The volume retained in the collection line was measured previously and was discarded. 5 ml was withdrawn directly into a container containing 40 ml of 2 mol/L sodium hydroxide solution (NaOH) for potentiometric titration analysis and 1 ml was withdrawn into a collection tube for total iron content analysis with a kit (K-6210) for iron measurement from CHEmetrics. Titration analyses were performed with a Metrohm Titrando 905 using 0.01 mol/L silver nitrate as titrant.

2.4. Immersion and weight loss tests

After the tests, the specimens were subjected to a chemical pickling procedure according to ASTM G1[21], obtaining the real weight loss. Corrosion rates were obtained according to ASTM G31-72[22]

3. Results and Discussions

3.1. Computational fluid dynamic simulations

3.1.1. Wall shear stress (τ_w)

The results obtained by numerical simulations of the testing design show a non-uniform distribution of instantaneous τ_w. Figure 3 show the distribution τ_w values on the surfaces of the simulated samples with baffles at 500 rpm (A) and
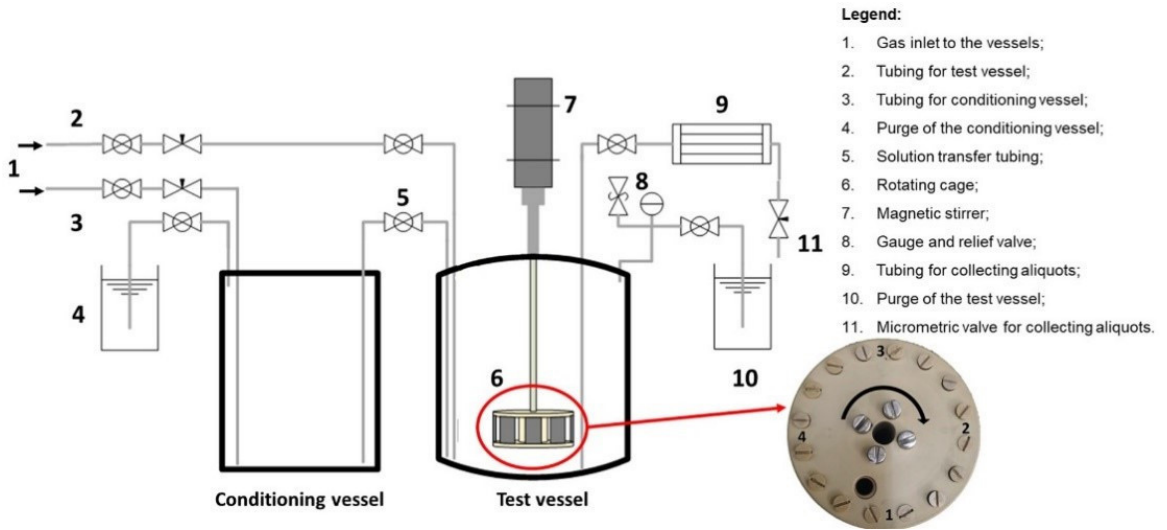
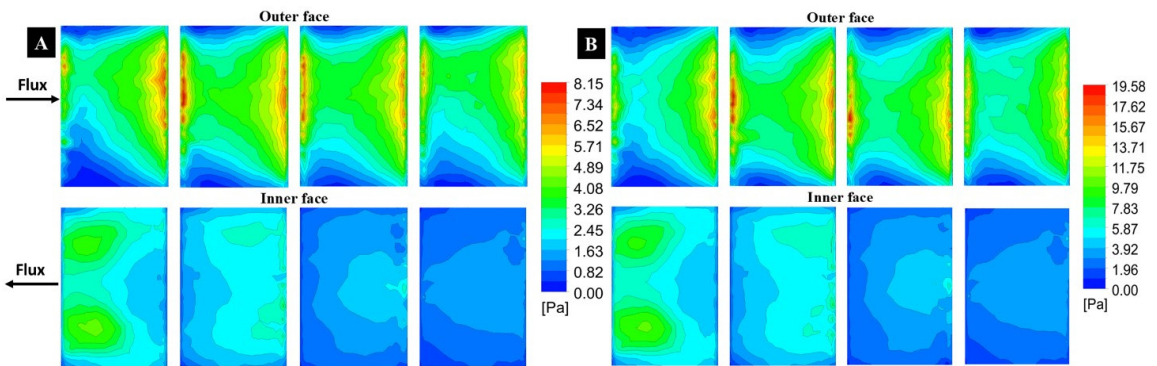**Figure 2.** Autoclave scheme used in the tests.

Figure 3. τ_w for RC with baffles on surfaces of the coupons, 500 rpm (A) and 800 rpm (B).

800 rpm (B). Figure 4 show the case results obtained for 500 rpm without baffles, simulated to assess the baffles influence on fluid dynamics. The figures represent the shear stresses on the samples by a color scheme, where regions in red represent the highest values, and regions in blue represent the lowest values. Each figure has its own scale of values.

Table 1 summarizes the maximum τ_w values found in the three cases and the value calculated by the Equation 1 (ASTM G170).

The maximum value of τ_w was 8.15 Pa in the RC simulations at 500 rpm with baffles (Figure 3A), while at 800 rpm (Figure 3B) this value increased to 19.58 Pa. The increase in rotation caused the increase in τ_w values, a fact that is already well grounded in the literature[20]. For the case where the GR was simulated without the baffles and 500 rpm (Figure 4), the maximum value of τ_w was 3.13 Pa on the samples edge, approximately 2.6 times lower than the case with baffles (8.15 Pa) (Table 1). The maximum values of τ_w, for the 3 cases, were detected in the region of half height of the coupons, that are in agreement with Senior et al.[16].

The values calculated by the Equation 1 were greater than the simulated values in all cases, this shows that the response

Table 1. Maximum τ_w values for 3 simulated cases.

Conditions	(CFD) τ_w max. (Pa)	(Equation) τ_w max. (Pa)
500 rpm with baffles	8.15	15.5
800 rpm with baffles	19.58	39.7
500 rpm without baffles	3.13	15.5

of a single value, and with a significant conservatism built in, from the standard test, is not sufficient for the complete understanding of the mechanisms in the RC.

The conservatism in corrosion rate values, for example, works as a safety factor for structures. However, this study and several works in the literature, show that this conservatism is excessive in the vast majority of times. Furthermore, Papavinasam et al.[20] presented, the still widely used equation, as a first approximation for his experimental apparatus. Which differs from most rotary cage vessels and autoclaves equipped with rotary cage that are currently used by various industries and research centers and cited in the paper.

CFD simulations have their proven efficiency in reproducing the actual physics of the problem, and unlike

the equation, it takes into account all the physical and geometric details of the simulated condition, and seeks the most exact reproducibility possible, of the laboratory test condition. Therefore, it is believed that the values obtained by CFD more accurately portray the actual fluid-dynamic stresses to which the samples are exposed. It is evident the need for a detailed parametric study to better approximate the available equations with each experimental test condition.

Considering that the only modification in both cases with vortex cutter (Figure 3) was the rotation of the RC, all specimens, on the external side, presented the same pattern of stress distribution. For RC with no baffles, the distribution of τ_w is also highly non-uniform and the patters of superficial distribution of τ_w is quite different when compared with RC with baffles.

According to these results, it is possible to observe that the baffles have strong impact both in magnitude and in distribution of the τ_w. These differences can be observed by simple comparison between Figures 3 and 4.

Ramachandran (2006) states that the flow over the coupons is closer to that of a flat plate moving at a slight angle of attack in a fluid. Due to that, the numerical results were validated from flat plane theory and showing an excellent coincidence between them.

The Figure 5 shows the velocity contours simulation results at 500 rpm and 800 rpm with baffles and without baffles with 500 rpm. All planes are located in the half height of the rotating cage. It is possible to observe a complex flow pattern, as typically in this kind of application. An important observation is related to the recirculation pattern created in the regions between baffles.

3.2. Equation discussion

Few studies exist with focus on improving the mathematical and geometric parameters of RC and shear stress calculation, in an attempt to propose changes in the models and equations. There is a gap that allows several studies on the subject.
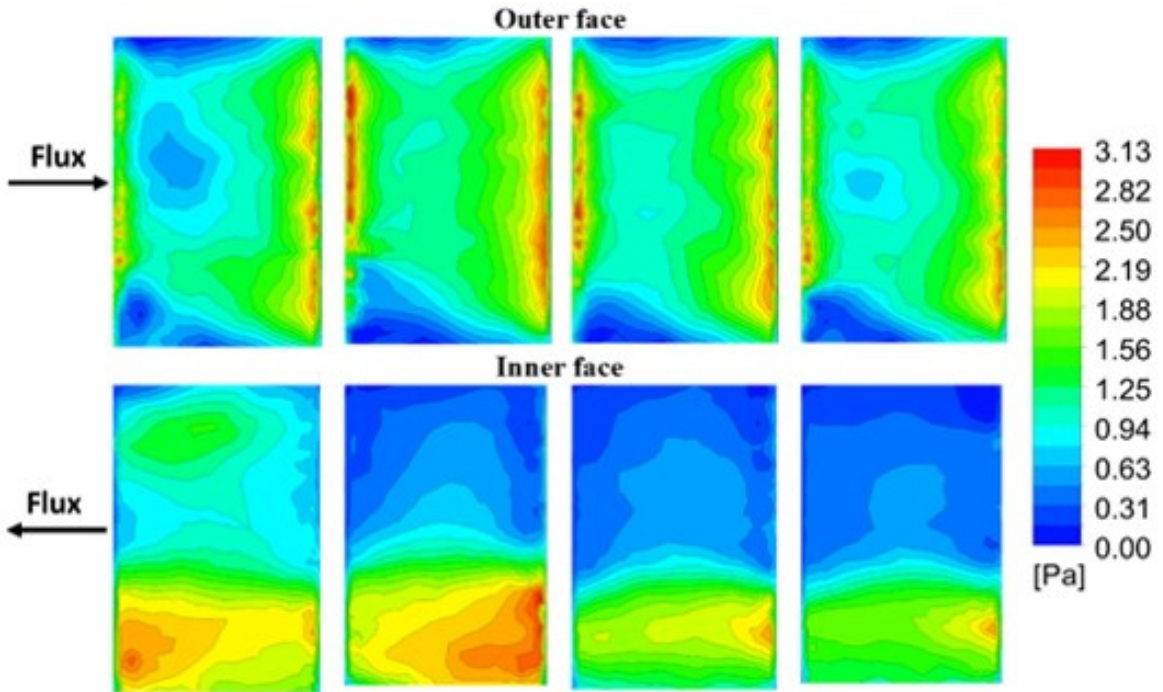

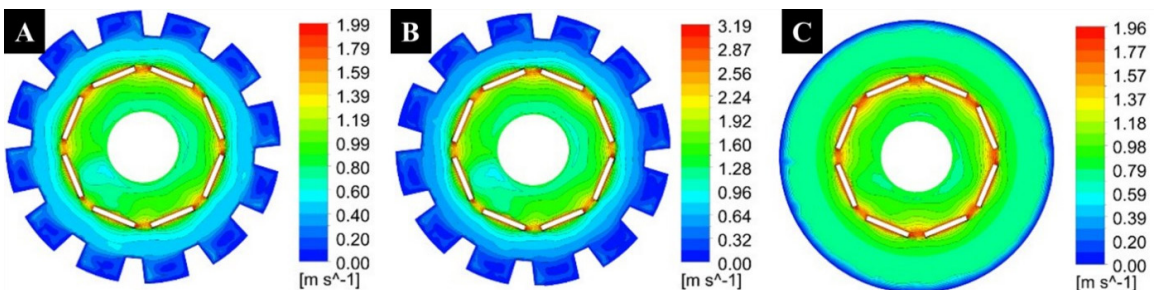**Figure 4.** τ_w for RC, 500 rpm with no baffles on surfaces of the coupons.

Figure 5. Velocity contours planes for the three studies cases: (a) 500 rpm with baffles, (b) 800 rpm with baffles (c) 500 rpm without baffles.

A detailed review showed that the equation for calculating the specimens wall stress in RC, proposed by Papavinasam et al.[20], is derived from the equation used for rotating cylinder electrodes, a methodology already established in the literature[23-25]. The tangential wall stress or wall shear stress (τ_w), for 2 concentric cylinders, the inner rotates at a speed n (in rpm) and the exterior is stationary, with the space between them filled by a fluid, a system similar to a rotating cylinder electrode assembly, can be determined by the classic Equation 3[26]:

$$\tau_w = \frac{f}{2}\rho u^2 \tag{3}$$

Where f is the Fanning friction coefficient of the fluid on the surface, ρ the density and u the tangential velocity in the wall of the inner cylinder (u = (2πn/60)r = ωr), with r the inner cylinder radius. Replacing u in Equation 3 has Equation 4:

$$\tau_w = \frac{f}{2}\rho r^2 \tag{4}$$

In experimental studies of corrosive mechanisms, when flow is turbulent (Re > 200), τ_w and the mass transfer coefficient (J_D) are variables that are closely related according to the Chilton-Colburn analogy[25,27,28], expressed by Equation 5:

$$J_D = \frac{f}{2} \tag{5}$$

This analogy is satisfactory in applications that do not have form drag forces, as happens in the internal pipe flow, and is valid for 2000 < Re < 300000 and 0.6 < Sc < 2.5. Sc is Schmidt's number[29]. The J_D and f relationship is considered valid and still used by numerous analytical and experimental works. Papavinasam[20] cited the work of Eisenberg and his collaborators[29] in your proposition. In the study, J_D results for five electrochemical systems are related to a f vs. Re graph, obtained from the Theodorsen and Regier studies[30]. The results presented prove a relationship between J_D and f, similar to that established by the Chilton-Colburn analogy (Equation 5). Figure 6 shows the point cloud that characterize the J_D and Re ratio for the five systems studied.

It is observed that in the range of 1000 < Re < 100000, the points can be adjusted, on a log-log scale, by Equation 6:

$$J_D = 0,0791 Re^{-0,3} \tag{6}$$

According to Chilton-Colburn analogy, valid for the study of corrosion processes, Equation 7 is:

$$J_D = \frac{f}{2} = 0,0791 Re^{-0,3} \tag{7}$$

Replacing Equation 7 in Equation 4, the wall shear stress in the determined by Equation 8, with Re to the cylinder (Equation 9):

$$\tau_w = 0,0791 Re^{-0,3}\rho r^2 \omega^2 \tag{8}$$

$$Re = \frac{2\rho u r}{\mu} \tag{9}$$

The modification steps of Equation 8 to Equation 1 were not found in the literature, where the only difference is the angular velocity (ω) exponent, from 2 to 2.3. Works used in the above deductions and by Papavinasam in their proposition of the RC equation make it clear that all approximations are valid for the specific conditions evaluated by them. Currently, the tests have been done in autoclaves, with variations in fluid volume, vessel diameter, rotation, presence of baffles, different cage models among other modifications[31-33], which makes it impossible to use Equation 1 as a prediction of specimens τ_w.
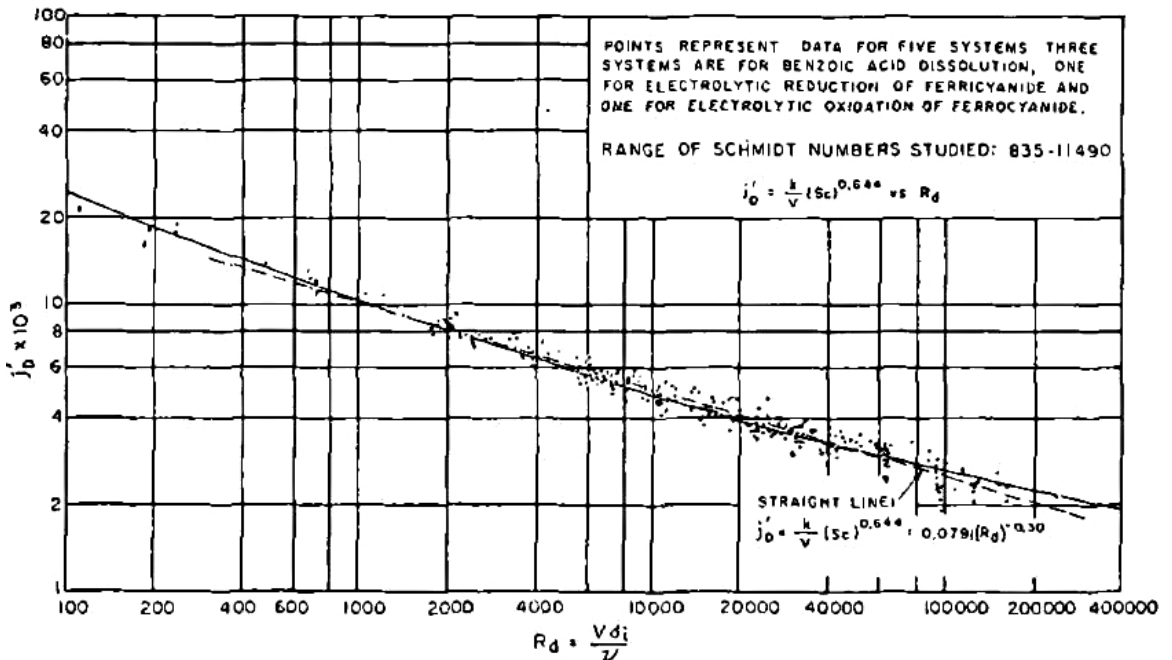

Figure 6. Correlation between J_D and Re for an internal cylinder in rotation. Points obtained in the 5 evaluated systems with the coefficient of friction (f/2)[29].

In addition to the need to adjust the τ_w equation for each specific condition, the ASTM G170 standard[19], through Equation 1, provides only a maximum value of τ_w generalizing all regions of all RC specimens, which according to CFD results (Figures 3 and 4) is not a representative value of the entire test. Several authors are dedicated to studying the factors that approximate the results obtained in laboratory tests with GR and the data observed in the real field conditions[16,34-38]. However, an equation or more appropriate experimental variation for the technique has not been proposed yet.

It is evident and proven the efficiency of this technique in internal corrosion FAC studies. However, it is also known the great conservatism embedded in the corrosion rate values obtained[37,39]. Among the factors responsible for this conservatism is the excessive corrosion that occurs at the specimens attack edges and the heterogeneous distribution of τ_w, especially on the internal faces of the samples (Figures 3 and 4). These exaggerated values imply excessive conservatism in material selections, corrosion inhibitors and operating conditions in the oil and gas industries[38].

3.3. Material characterization

Figure 7 shows API X65 carbon steel micrographs with 100x and 1000x magnifications. It is possible to observe a ferritic/pearlitic microstructure, with ferrite and perlite grains in a homogeneous distribution (Figure 7A). Predominantly, the fine perlite colonies are located in the ferrite grain boundaries, which present an irregularity in sizes and shapes (Figure 7B).
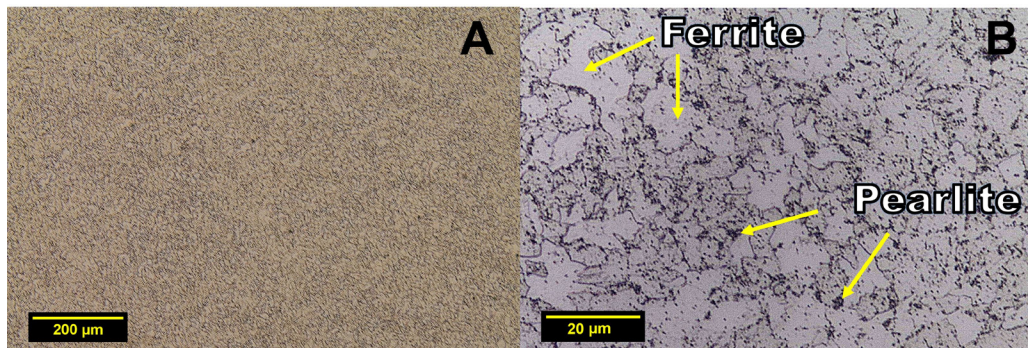
Several authors report the influence of the material microstructure on the corrosion rate and the precipitation of corrosion products on the surface[40,41]. According to the literature[40,42-46], cementite presents a more positive potential than the ferritic phase. This fact generates a micro galvanic couple between the Fe_3C grains (cathodic side), and the ferrite (α-Fe) grains (anodic side), and promotes a preferential dissolution of α-Fe.

The preferential decay of ferrite contributes to the precipitation/nucleation of corrosion products because it increases the release of Fe^{2+} into solution.

Studies such as the one by Di Bonaventura et al.[47], show that due to dissolution of the ferrite regions, portions of Fe3C are exposed and receive direct mechanical action from the flow.

The cementite is brittle, however, for the practical conditions encountered, the forces of the flow are not able to remove the cementite from the surface of the material. In addition, cathodic reactions tend to occur on this remaining cementite structure. Where sulfide and carbonate films are initially deposited[45,48].

3.4. Autoclave tests

Figure 8 shows the impact of using the baffles on the flow pattern inside the vessel in the 2 evaluated rotations (500 and 800 rpm).

Several authors[16,49,50] also report a vortex increase with increased rotation. Without the baffles, the tendency is that this vortex to penetrate inside the cage.

Figure 7. API X65 carbon steel microstructure. (A) 100 x e (B) 1000x.
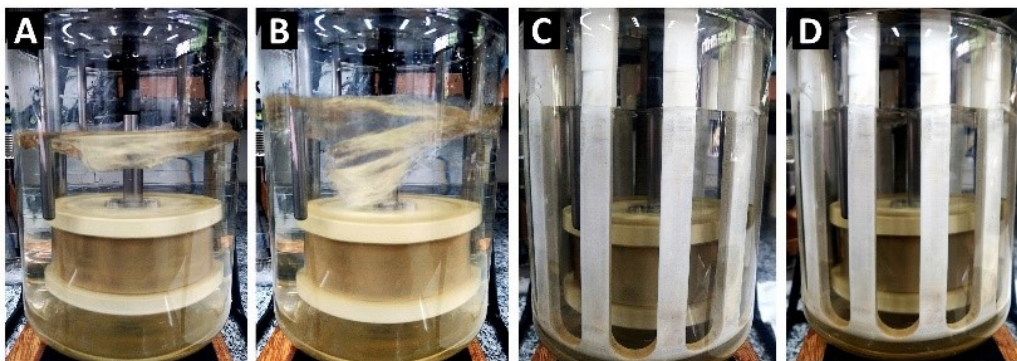

Figure 8. Influence of baffles on the formed vortex. 500 rpm and 800 rpm without baffles (A and B), 500 rpm and 800 rpm with baffles (C and D).

Papavinasam[49], divides flow patterns into four regions with respect to the vortex formed:

1. Homogeneous zone: The vortex width and height increase as rotation increases.
2. Wall affected zone: The vortex height continues to increase, but the width is already limited by the vessel wall.
3. Turbulent zone: The vortex penetrates the cage and creates a turbulent flow with mixing between the liquid and gas phases.
4. Top cover affected zone: The liquid level rises and reaches the vessel cover, thereby a recirculation and a major change in the flow pattern.

It is possible to observe in Figure 8 the baffles efficiency in not allowing the vortex evolution and penetration inside the cage. From these results, all tests will be performed with baffles, which improves the homogeneity of the fluid inside the autoclave[28,36].

3.5. Potentiometric titration, Measurement of iron content and pH evolution

Figure 9 shows the evolution of H_2S concentration values, generated through the sodium thiosulfate reaction, pH and total iron concentration in the solution over the 25 h of immersion.

H_2S concentrations generated (Figure 9A) prove the efficiency of the generation of this through the sodium thiosulfate reaction, as proposed by Tsujikawa[51]. Dependence on H_2S generation with subtract corrosion is evident by the fact that 800 rpm tests showed higher values than tests at 500 rpm. The values found for the 2 conditions tried to a stable level after the first hours of testing.

pH (Figure 9B) has a significant increase in the first hour of immersion, showing that the corrosive mechanism alters the studied environment pH. The total iron content shown in Figure 9C suggests a greater aggressiveness of the 800 rpm tests, which presented higher Fe values after 12 h and 25 h of immersion. These results are in accordance with Rogowska et al.[52] that relate after the hydradiation of CO_2 and with the evolution of the corrosive mechanisms, the release of Fe^{2+} and the increase of CO_3^{2-} concentration contribute to the increase of the pH in the medium, as can be seen in the Figure 9B.

The iron content reduction shown in Figure 9C, over the immersion time, was possibly due to the formation reactions of corrosion products that consume Fe^{2+}. Subsequent results

showed that the 500 rpm tests showed a greater number of adhered products in surfaces.

1 L of solution was used inside the autoclave in the experiments, and the results (Figure 9A and B) proved a change in the physical-chemical properties of the solution. In the field, the medium does not change significantly, since the flow, constantly "renews" the solution in contact with a substrate area[53]. Becoming clear the need to improve the technique of tests with RC in autoclaves, in order to renew the electrolyte inside the vessel[54,55].

3.6. Surface characterization

Immediately after the autoclave was opened, the specimens were cleaned with acetone and dried with hot air. Figures 10 and 11 show the external and internal sides of the 4 specimens tested in each rotation with baffles (500 rpm and 800 rpm respectively)

It is clear the non-uniformity of corrosion on the inner side and on the outside, as well as the difference in the corrosion products formation within the same sample.

DRX analyses were performed on both sides of each sample for the characterization of corrosion products. The XRD analyses are shown in Figure 12.

The samples tested at 500 rpm presented a dense and uniform film on the outer face and a mixture of different corrosion products. In samples macrographs (Figure 10) it is possible to observe a dense gray film characterized as sulfide films by DRX analyses (Figure 12A) and regions with the darker corrosion product predominance on the internal side of the specimens, possibly being iron carbonate and chukanovite. These sweet corrosion products appear with peaks of greater intensity on the inner face of the DRX analysis (Figure 12B). Sample 1 presented lighter film deflating on the outside.

The 500 rpm tested samples present a large amount of sulfides, in addition to chukanovite, siderite and oxides as magnetite, possibly formed during disassembly and storage process until the DRX analyses.

A brittle film of iron sulfide layer in its different morphologies have possibly contributed to the lowest corrosion rate values observed in this condition.

According to Wen and his collaborators[56], carbon steels when in contact with an H_2S containing environment and water, immediately form an adherent film on the anodic material surface, as well as found in previous works[57]. The various corrosion products forms tend to be mainly non-stoichiometric iron sulfide compounds. H_2S concentrations
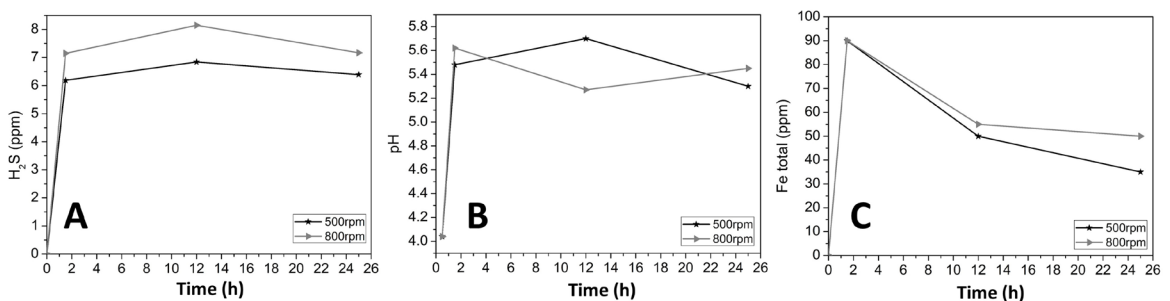

Figure 9. H_2S concentration values (A), pH (B) and total iron (C) during the immersion period in the 2 rotations.
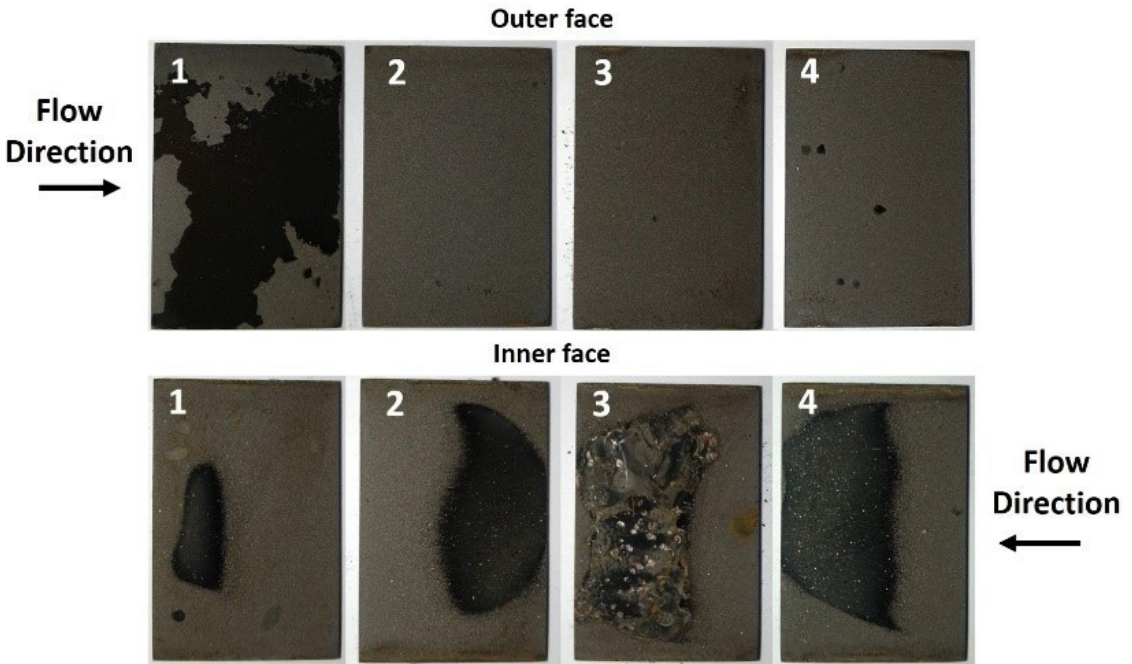
Figure 10. Specimens after 25 h of immersion at 500 rpm, before the pickling process.
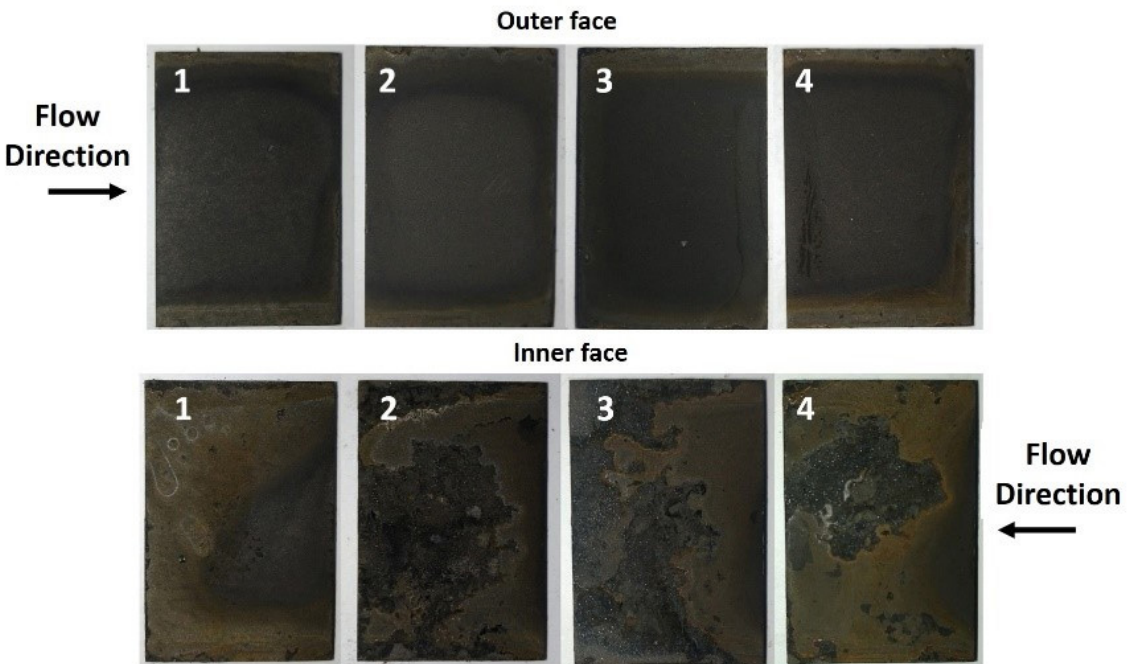

Figure 11. Specimens after 25 h immersion at 800 rpm, before the pickling process.

and temperature variations result in major morphology and crystalline structure changes[58].

The images of the specimens exposed to 800 rpm (Figure 11) make clear the difference between the fluid dynamics outside and inside the rotating cage, in accordance with CFD results (Figure 3B). It is possible to note that the

outside faces do not present any adherent film formation, while a heterogeneous corrosion products film covers the inner side (Figure 11).

On the internal samples surfaces, large regions were noticed (Figure 11) containing dark crystals similar to iron carbonate and chukanovite crystals presented in the
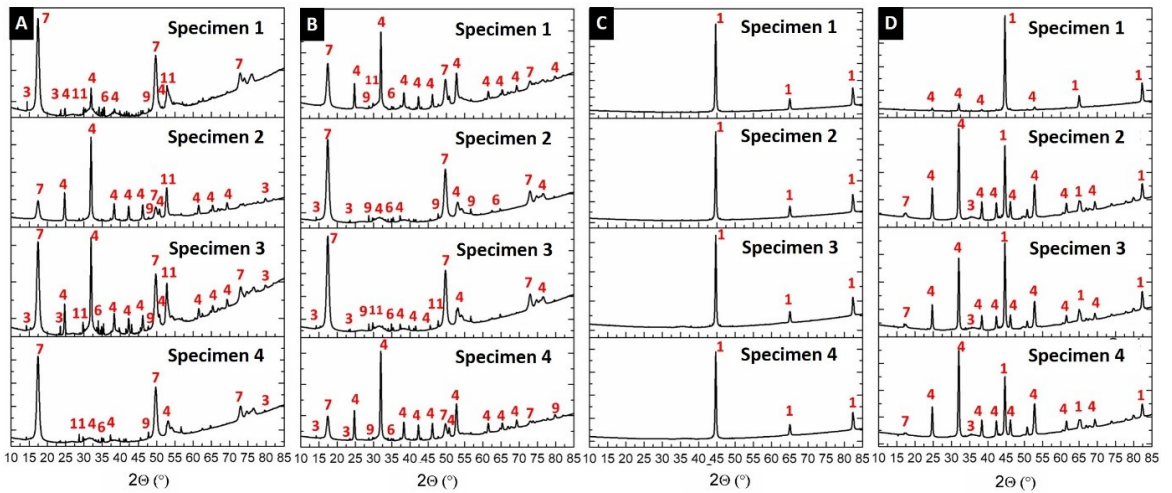
Figure 12. DRX analysis for the 4 samples tested at 500 rpm, external (A) and internal (B) and 800 rpm external (C) and internal (D). (1- Ferrite, 2- Cementite, 3- Chukanovite, 4- Siderite, 5- Hematite, 6- Magnetite, 7- Mackinawite, 8- Greigite, 9- Pyrite, 10- Pyrrhotite, 11- Smythite, 12- Trolite, 13- Marcasite).
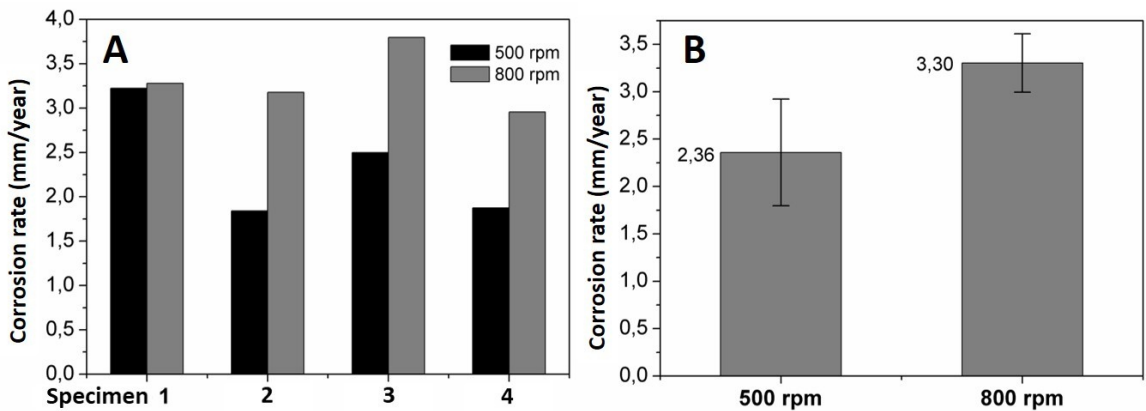
Figure 13. Corrosion rate for each specimen (A) and average value for each rotation (B).

literature[57,59,60] and found in DRX analyses (Figure 12D). These crystals preferentially formed where the iron sulfide film failed or presented pores and cracks.

All the samples tested at 800 rpm (Figure 11) presented little or no adhered corrosion products on the external face. Only ferrite was identified by the DRX, this phase is present in the steel microstructure (Figure 7).

The inner faces presented predominantly iron carbonate, and few indications of macknawite, suggesting that the increase in rotation may have impaired the adhesion of sulfide films, consequently favored the $FeCO_3$ precipitation (Figure 11 and 12-D). Probably due to increased rotation and high τ_w values (Figure 3), the film of iron sulfide, naturally brittle and fragile[61,62], may have been released, allowing a greater carbonate crystals formation. The CFD results corroborate these assertions, since the wall shear stresses in the 800 rpm tests were 2,6 times higher than 500 rpm.

3.7. Weight loss and corrosion rate

After characterization, the pickling process provided the real weight loss and the corrosion rate of each sample (Figure 13A). Figure 13B shows the mean corrosion rate values for the 2 evaluated rotations.

The increase in rotation generated an increase in corrosion rate, this result was already expected and already well discussed in the literature[35,37,63], CFD results (Figures 3 and 4) had already suggested this behavior.

The specimens 1 and 3 (Figure 13A) presented higher corrosion rate for the 2 rotations, which makes clear the influence of shear stress. Figure 3 and 4 shows the regions with the highest τ_w value due to the internal flow imposed by the single hole in the cage discs. This result is in line with the work in literature[16,35] that also showed this difference, and the cage geometry influence on the corrosion rate.

The graph of Figure 13A and the large standard deviation in Figure 13B clearly show the non-uniformity of corrosion

rate values for specimens in different positions in the RC. This variation compromises the conclusions obtained with the technique, emphasizing the need to improve the experimental methodology.

4. Conclusions

- It is evident the need for an update in the ASTM G170 equation. As seen, the equation currently used is limited to the geometry and conditions used by the author for such a proposition;
- The RC evaluated by CFD presented a non-uniformity in the distributions of τ_w, having the influence of this non-uniform distribution on the corrosion rate, proven by the surfaces characterization results;
- The environment physicochemical analyses showed an increase in pH and Fe and justify the need to renew the test solution over the immersion period;
- The increase in RC rotation promotes an increase in average and maximum τ_w, thus increasing the corrosion rate. This increase may be due to the negative impact of the higher rotation alum in the formation and adhesion of corrosion products;
- The results of CFD and DRX show that corrosion products have suffered great influence from the τ_w distributions. FeS, naturally brittle and fragile, tends to detach in regions with the highest incidence of flow, enabling nucleation and or precipitation of $FeCO_3$ films in these regions.

5. References

1. Bandeira, M. C. E., Spigarollo, D., Moreira, R. M. & Mattos, O. R. Influence of small amount of H_2S on the CO_2 corrosion of carbon steel at oil production conditions. In: INTERCORR 2016; 2016; Búzios, RJ. Proceedings. Rio de Janeiro: ABRACO; 2016.
2. Kahyarian A, Brown B, Nesic S. Discussion on "Electrochemistry of CO_2 corrosion of mild steel: effect of CO_2 on iron dissolution reaction" by A. Kahyarian, B. Brown, S. Nesic, [Corros. Sci. 129 (2017) 146–151]. Corros Sci. 2018;133:417-22.
3. Almeida TC, Bandeira MCE, Moreira RM, Mattos OR. New insights on the role of CO_2 in the mechanism of carbon steel corrosion. Corros Sci. 2017. http://dx.doi.org/10.1016/j.corsci.2017.02.016.
4. Wei L, Pang X, Zhou M, Gao K. Effect of exposure angle on the corrosion behavior of X70 steel under supercritical CO_2 and gaseous CO_2 environments. Corros Sci. 2017;121:57-71.
5. Kahyarian A, Brown B, Nesic S. Mechanism of CO_2 corrosion of mild steel: a new narrative. In: CORROSION 2018; 2018; Phoenix, Arizona. Proceedings. Texas: NACE; 2018.
6. Zeng Z, Lillard RS, Cong H. Effect of salt concentration on the corrosion behavior of carbon steel in CO_2 environment. Corrosion. 2016;72(6):805-23.
7. Jin P, Robbins W, Bota G. Effect of sulfur compounds on formation of protective scales in naphthenic acid corrosion in non-turbulent flow. Corros Sci. 2018;131:223-34.
8. Zhang H, Pang X, Gao K. Localized CO_2 corrosion of carbon steel with different microstructures in brine solutions with an imidazoline-based inhibitor. Appl Surf Sci. 2018;442:446-60. http://dx.doi.org/10.1016/j.apsusc.2018.02.115.
9. Elgaddafi R, Ahmed R, Shah S. Modeling and experimental studies on CO_2-H_2S corrosion of API carbon steels under high-pressure. J Petrol Sci Eng. 2017;156:682-96.
10. Barker R, Burkle D, Charpentier T, Thompson H, Neville A. A review of iron carbonate ($FeCO_3$) formation in the oil and gas industry. Corros Sci. 2018;142:312-41. http://dx.doi.org/10.1016/j.corsci.2018.07.021.
11. Umoren SA, Solomon MM, Saji VS. Corrosion inhibitors for sour oilfield environment (H_2S corrosion). In: Saji VS, Umoren SA, editors. Corrosion inhibitors in the oil and gas industry. Weinheim: Wiley-VCH; 2020. p. 229-54. http://dx.doi.org/10.1002/9783527822140.ch8.
12. Yin ZF, Zhao WZ, Bai ZQ, Feng YR, Zhou WJ. Corrosion behavior of SM 80SS tube steel in stimulant solution containing H_2S and CO_2. Electrochim Acta. 2008;53(10):3690-700. http://dx.doi.org/10.1016/j.electacta.2007.12.039.
13. Gayosso MJH, Olivares GZ, Fragoso SB, del Valle GEB, Oidor DMG, Gómez VÁR. Corrosion behavior of API 5L X52 steel under high concentrations of H_2S/CO_2 Gases. Mater Sci Appl. 2016;07(10):623-43.
14. Cabrera-Sierra R, Cosmes-López LJ, Castaneda-López H, Calderón JT, Hallen López JM. Corrosion studies of carbon steel immersed in NACE brine by weight loss, EIS and XRD techniques. Int J Electrochem Sci. 2016;11:10185-98.
15. Ajmal TS, Arya SB, Udupa KR. Effect of hydrodynamics on the flow accelerated corrosion (FAC) and electrochemical impedance behavior of line pipe steel for petroleum industry. Int J Press Vessels Piping. 2019;174:42-53.
16. Senior N, Boisvert P, Runstedtler A, Arafin M. Simulating liquid pipeline flow using the rotating cage method. Corrosion. 2015;2015:13.
17. Viçosa IN. Construção e teste de um sistema de 'Rotating Cage' para realização de medidas eletroquímicas em altas tensões de cisalhamento para avaliação da corrosão em aço carbono utilizado em dutos de transporte de petróleo [projeto de graduação]. Rio de Janeiro: Universidade Federal do Rio de Janeiro; 2015.
18. Arismendi Florez JJ, Ferrari JV. Fluid flow effects on CO_2 corrosion: a review of applications of rotating cage methodology. Anti-Corros Methods Mater. 2019;66(4):507-19.
19. ASTM: American Society for Testing and Materials. ASTM G170: standard guide for inhibitors in the laboratory. West Conshohocken: ASTM; 2012. p. 1-16.
20. Papavinasam S, Revie RW, Attard M, Demoz A, Sun H, Donini JC, et al. Inhibitor selection for internal corrosion control of pipelines. In: CORROSION 2000; 2000; Orlando, Florida. Proceedings. Texas: NACE; 2000.
21. ASTM: American Society for Testing and Materials. ASTM-G1: standard practice for preparing, cleaning, and evaluating corrosion test: significance. West Conshohocken: ASTM; 1999.
22. ASTM: American Society for Testing and Materials. ASTM G31-72: standard practice for laboratory immersion corrosion testing of metals. West Conshohocken: ASTM; 2004.
23. Silverman DC. Rotating cylinder electrode for velocity sensitivity testing. Corrosion. 1984;40(5):220-6.
24. Gabe DR. The rotating cylinder electrode. J Appl Electrochem. 1974;4(2):91-108.
25. Efird KD, Wright EJ, Boros JA, Hailey TG. Correlation of steel corrosion in pipe flow with jet impingement and rotating cylinder tests. Corrosion. 1993;49(12):992-1003.
26. White FM. Mecânica dos fluidos. Porto Alegre: AMGH; 2011.
27. Silverman DC. Rotating cylinder electrode-geometry relationships for prediction of velocity-sensitive corrosion. Corrosion. 1988;44(1):42-9. http://dx.doi.org/10.5006/1.3582024.
28. Runstedtler A, Huang J, Boisvert P, Senior N. Parametric wall shear stress characterization of the rotating cage test method. Corrosion. 2006;41:106-8.
29. Eisenberg M, Tobias CW, Wilke CR. Ionic mass transfer and concentration polarization at rotating electrodes. J Electrochem Soc. 1954;101(6):306-20.

30. Theodorsen T, Regier A. Experiments on drag of revolving disks, cylinders, and streamline rods at high speeds. Washington: NASA; 1945. p. 367-84.

31. Zeng Y, Shi C, Arafin M, Zavadil R. Influence of impurity hydrogen sulfide on the corrosion performance of pipeline steels in supercritical carbon dioxide stream. In: Corrosion 2016 Conference & Expo; 2016; Houston. Proceedings. Texas: NACE; 2016.

32. Zhao Y, Li X, Zhang C, Zhang T, Xie J, Zeng G, et al. Investigation of the rotation speed on corrosion behavior of HP-13Cr stainless steel in the extremely aggressive oilfield environment by using the rotating cage test. Corros Sci. 2018;145:307-19.

33. Hirano S, Sunaba T, Al Jaberi M, Al Alawi F. Evaluation of corrosion inhibitor performance under high temperature/ high salinity sweet conditions. In: International Petroleum Exhibition & Conference; 2018; Abu Dhabi. Proceedings. Abu Dhabi: Society of Petroleum Engineers; 2018. http://dx.doi.org/10.2118/193016-ms.

34. Ramachandran P. Numerical simulation of the rotating cage problem. In: 33rd National and 3rd International Conference on Fluid Mechanics and Fluid Power; 2017; Bombay. Proceedings. Bombay: IIT Bombay; 2017.

35. Vera JR, Parsi M, Kara M, Sharma P, Li X, Jatale A. Appropriate rotating cage speed for testing inhibitors under field simulated flow conditions. In: CORROSION 2017; 2017; New Orleans, Louisiana. Proceedings. Texas: NACE; 2017.

36. Kumar A, Ling S, Pacheco JL, Desai SK, Reddy RV. Effects of rotating cage autoclave design on shear stress and flow pattern. Corros. 2013;2013:1-13.

37. Spigarollo D, Bandeira M, Nogueira IV, Moreira R, Mattos OR. Bringing new functionalities to rotating cage autoclave assembly. In: INTERCORR 2018; 2018; São Paulo, SP. Proceedings. Rio de Janeiro: ABRACO; 2018.

38. Diehl B No, Oliveira J, Baptista I, Bandeira, M. Influência do teor de água na avaliação da corrosão de colunas de produção por meio da técnica de gaiola rotatória. In: INTERCORR 2016; 2016; Búzios, RJ. Proceedings. Rio de Janeiro: ABRACO; 2016.

39. Bandeira MCE, Moreira R, Assunção F, Mattos O, Vaz G, Oliveira J, et al. Carbon steel corrosion on production environment, evaluating the impact of CO_2 partial pressure, BSW and oil characteristics on tubular life extend. In: Corrosion 2021 Conference & Expo; 2021. Proceedings. Texas: NACE; 2021.

40. Farelas F, Galicia M, Brown B, Nesic S, Castaneda H. Evolution of dissolution processes at the interface of carbon steel corroding in a CO_2 environment studied by EIS. Corros Sci. 2010;52(2):509-17.

41. Zhang GA, Cheng YF. Corrosion of X65 steel in CO_2-saturated oilfield formation water in the absence and presence of acetic acid. Corros Sci. 2009;51(8):1589-95.

42. Ezuber HM. Influence of temperature and thiosulfate on the corrosion behavior of steel in chloride solutions saturated in CO_2. Mater Des. 2009;30(9):3420-7.

43. Kappes MA. Evaluation of thiosulfate as a substitute for hydrogen sulfide in sour corrosion fatigue studies [thesis]. Ohio: Ohio State University; 2011.

44. Sun JB, Zhang GA, Liu W, Lu MX. The formation mechanism of corrosion scale and electrochemical characteristic of low alloy steel in carbon dioxide-saturated solution. Corros Sci. 2012;57:131-8.

45. Tang J, Shao Y, Guo J, Zhang T, Meng G, Wang F. The effect of H_2S concentration on the corrosion behavior of carbon steel at 90°C. Corros Sci. 2010;52(6):2050-8.

46. Zhao W, Zou Y, Matsuda K, Zou Z. Characterization of the effect of hydrogen sulfide on the corrosion of X80 pipeline steel in saline solution. Corros Sci. 2016;102:455-68.

47. Di Bonaventura M, Brown B, Singer M, Nesic S. Effect of flow and steel microstructure on the formation of iron carbonate. In: CORROSION 2018; 2018; Phoenix, Arizona. Proceedings. Texas: NACE; 2018.

48. Farelas F, Brown B, Nesic S. Iron carbide and its influence on the formation of protective iron carbonate in CO_2 corrosion of mild steel. In: CORROSION 2013; 2013; Orlando, Florida. Proceedings. Texas: NACE; 2013.

49. Papavinasam, S. Rotating cage and jet impingement techniques. In: Yang L, editor. Techniques for corrosion monitoring. London: Woodhead Publishing; 2008. p. 323-44.

50. Papavinasam S, Attard M, Revie RW, Bojes J. Rotating cage: a compact laboratory methodology for simultaneously evaluating corrosion inhibition and drag reducing properties of chemicals. In: CORROSION 2002; 2002; Denver, Colorado. Proceedings. Texas: NACE; 2002.

51. Tsujikawa S, Miyasaka A, Ueda M, Ando S, Shibata T, Haruna T, et al. Alternative for evaluating sour gas resistance of low-alloy steels and corrosion-resistant alloys. Corrosion. 1993;49(5):409-19.

52. Rogowska M, Gudme J, Rubin A, Pantleon K, Ambat R. Effect of Fe ion concentration on corrosion of carbon steel in CO_2 environment. Corros Eng Sci Technol. 2016;51(1):25-36.

53. Zhong X, Brown B, Li W, Nesic S, Singer M. How to maintain a stable solution chemistry when simulating CO_2 corrosion in a small volume laboratory system. In: Corrosion 2016 Conference & Expo; 2016; Houston. Proceedings. Texas: NACE; 2016.

54. Ascencio M, Pekguleryuz M, Omanovic S. An investigation of the corrosion mechanisms of WE43Mg alloy in a modified simulated body fluid solution: the effect of electrolyte renewal. Corros Sci. 2015;91:297-310.

55. Moreira R, Nascimento C, Bandeira M, Mattos O. Influência da renovação de meio corrosivo no comportamento do aço X65 quanto a corrosão em meios de CO_2 e H_2S. In: INTERCORR 2018; 2018; São Paulo, SP. Proceedings. Rio de Janeiro: ABRACO; 2018.

56. Wen X, Bai P, Luo B, Zheng S, Chen C. Review of recent progress in the study of corrosion products of steels in a hydrogen sulphide environment. Corros Sci. 2018;139:124-40.

57. Souza RC, Santos BAF, Gonçalves MC, Mendes EP Jr, Simões TA, Oliveira JR, et al. The role of temperature and H_2S (thiosulfate) on the corrosion products of API X65 carbon steel exposed to sweet environment. J Petrol Sci Eng. 2019;180:78-88.

58. Shi F, Zhang L, Yang J, Lu M, Ding J, Li H. Polymorphous FeS Corrosion products of pipeline steel under highly sour conditions. Corros Sci. 2016;102:103-13.

59. Ko M, Ingham B, Laycock N, Williams DE. In situ synchrotron X-ray diffraction study of the effect of chromium additions to the steel and solution on CO_2 corrosion of pipeline steels. Corros Sci. 2014;80:237-46.

60. Pandarinathan V, Lepková K, van Bronswijk W. Chukanovite $(Fe_2(OH)_2CO_3)$ identified as a corrosion product at sand-deposited carbon steel in CO_2-saturated brine. Corros Sci. 2014;85:26-32.

61. Kahyarian, A., Brown, B. N. & Nesic, S. CO_2 corrosion, H_2S corrosion, organic acid corrosion: a unifying perspective on corrosion mechanisms in weak acid solutions. In: CORROSION 2019 Conference & Expo; 2019; Nashville, Tennessee. Proceedings. Texas: NACE; 2019.

62. Lee K-LJ. A mechanistic modeling of CO_2 corrosion of mild steel in the presence of H_2S. Ohio: Ohio University; 2004.

63. Papavinasam S, Doiron A, Revie RW. Effect of rotating cage geometry on flow pattern and corrosion rate. Corrosion. 2003;2003:1-19.